Electrochimica Acta 574 (2026) 149408

Contents lists available at ScienceDirect

Electrochimica Acta

journal homepage: www.journals.elsevier.com/electrochimica-acta

Analysis of low-frequency impedance processes in segmented PEM fuel cells

Philipp Oppek [a,*], Kersten Schwab [a], Tobias Goosmann [a], Sebastian Raab [a], Yannick Fischer [b], Mischa Geörg [b], Tatyana Reshetenko [c], André Weber [a]

[a] Institute for Applied Materials (IAM-ET), Karlsruhe Institute of Technology (KIT), Adenauerring 20b, Karlsruhe, 76131, Germany
[b] GFS Fuel Cells GmbH, Auf der Trift 3, Saarbrücken, 66127, Germany
[c] Hawaii Natural Energy Institute (HNEI), University of Hawaii, 1680 East-West Road, Honolulu, HI, 96822, USA

ARTICLE INFO

Keywords:
Polymer electrolyte membrane fuel cell
Electrochemical impedance spectroscopy
Distribution of relaxation times
Segmented cell
Low-frequency gas transport processes
Along-the-channel gradients

ABSTRACT

Under technically relevant air-fed polymer electrolyte membrane fuel cell (PEMFC) operation, the low-frequency impedance response is shaped by overlapping oxygen-transport processes along the cathode channel and through the porous gas diffusion layer (GDL), microporous layer (MPL), and cathode catalyst layer (CCL). Local ionomer hydration and liquid-water accumulation further modify these transport processes. In this study, these low-frequency contributions are resolved locally using an along-the-channel segmented PEMFC by combining sequential segment-wise electrochemical impedance spectroscopy (EIS) with subsequent distribution of relaxation times (DRT) analysis. Targeted variations in inert gas, cathode stoichiometry, current density, and relative humidity were evaluated together with along-the-channel current-density distributions, allowing two distinct low-frequency processes, P_{LF1} and P_{LF2}, to be separated over the investigated operating window. The results show that the relaxation frequency of the lower low-frequency peak, P_{LF1}, depends primarily on channel-gas velocity. Its polarization contribution is additionally influenced by oxygen depletion and oxygen transport along the channel. The higher low-frequency peak, P_{LF2}, is governed mainly by local through-plane oxygen transport through the GDL, MPL, and CCL and responds strongly to the effective oxygen diffusion coefficient, local oxygen availability, local current density, and water-modified transport conditions in the porous cathode. These findings establish a mechanistic distinction between a predominantly channel-related low-frequency contribution and a predominantly local through-plane oxygen-transport contribution in the porous cathode, providing a physically informed basis for interpreting low-frequency impedance signatures under technically relevant PEMFC operating conditions.

1. Introduction

Polymer electrolyte membrane fuel cells (PEMFCs) are regarded as a promising technology for efficient, low-emission power generation in high-power applications, including heavy-duty transport and stationary energy systems. For such applications, maintaining uniform local operating conditions across the fuel-cell stack is essential for achieving high performance and durability [1,2].

Automotive fuel-cell stacks typically employ long, parallel straight-channel flow fields and operate with humidified hydrogen and air, with only limited oxygen excess at the cathode, corresponding to cathode stoichiometries typically below 2 [3–5]. Under these conditions, along-the-channel gradients especially in reactant availability, humidity and liquid water accumulation are unavoidable [4,6]. These gradients modify the local electrochemical state and internal resistances and thereby govern both the spatial current-density distribution and the overall cell performance. Under these conditions, oxygen transport from the cathode channel through the porous media to the catalyst layer becomes a key performance factor. At the same time, oxygen depletion and water accumulation develop from inlet to outlet.

Electrochemical impedance spectroscopy (EIS), especially when combined with subsequent distribution of relaxation times (DRT) analysis, is a powerful tool to separate overlapping PEMFC loss contributions by their characteristic time constants. However, interpreting the low-frequency part of the impedance response remains particularly difficult, because it contains contributions from mass transport and water-related processes, that can overlap both within the catalyst layer and along the gas channel [7–10]. This ambiguity is especially relevant for long air-fed channels. Under low-stoichiometry operation, the local oxygen mole fraction can decrease from below the dry-air value of 21%

* Corresponding author.
E-mail address: Philipp.oppek@kit.edu (P. Oppek).

https://doi.org/10.1016/j.electacta.2026.149408
Received 19 March 2026; Received in revised form 23 June 2026; Accepted 25 June 2026
Available online 25 June 2026

at the humidified inlet to around 10% or less near the outlet. Water-vapor dilution and liquid-water accumulation further intensify this effect [11–13].

Although the low-frequency response is often treated as a single oxygen-transport peak, experiments and modeling show that multiple transport mechanisms can overlap in time and merge into a composite low-frequency signature [14,15]. Under automotive-relevant humidified hydrogen /air operation with long straight channels and low cathode stoichiometry, oxygen transport is affected not only by through-plane diffusion, but also by convection and oxygen depletion along the cathode channel [7,16,17]. Schneider et al. showed that AC-induced oxygen concentration oscillations are not confined to the porous cathode, but extend into the gas channels and couple downstream by forced convection, producing an additional low-frequency contribution [18]. Consistently, the characteristic time constant of the low-frequency arc varies strongly with cathode air-flow velocity and stoichiometry, but approaches a through-plane-transport limit at high flow rates [19]. Analytical work further predicts separate channel and porous-layer contributions, or a merged peak when their time scales overlap [17,20,21]. Thus, under stack-relevant conditions, the low-frequency "mass-transport" peak cannot be assigned to a single through-plane diffusion process, but may reflect multiple overlapping processes in the gas channel and porous cathode [22].

Resolving low-frequency impedance processes under realistic along-the-channel gradients therefore requires a physically informed and spatially resolved approach. An along-the-channel segmented cell is particularly suitable for this purpose because it captures the progressive oxygen depletion and water accumulation typical of long air-fed stack channels [19]. In combination with segmented current-density measurements and local impedance analysis, it enables the spatially resolved correlation of local electrochemical response with channel position [16,23,24]. This makes it possible to distinguish channel-scale effects from predominantly local oxygen transport in the porous cathode.

In the present work, a segmented PEMFC with a long straight-channel cathode flow field is used to resolve low-frequency impedance processes locally under technically relevant air-fed operation. Spatially resolved current-density measurements are combined with local EIS and DRT analysis. Targeted variations in inert gas type, cathode stoichiometry, current density, and relative humidity are applied to identify the governing transport processes and their domains. To obtain locally representative spectra with minimized upstream coupling, the impedance is measured by sequential segment-wise excitation.

Using this approach, two distinct low-frequency processes are identified and tracked systematically as a function of operating condition and channel position. The aim of this work is to establish their characteristic parameter dependencies and to distinguish between a predominantly local through-plane oxygen-transport contribution in the porous cathode and a predominantly channel-related low-frequency contribution associated with oxygen depletion along the cathode channel due to electrochemical consumption and convective gas transport.

2. Through-plane and along-the-channeloxygentransport

A compact formal starting point for oxygen transport in both the channel and porous cathode domains is the local steady convection–diffusion–reaction balance for oxygen (species α),

$$\frac{\partial}{\partial_{x_i}} * \left(- D_\alpha \frac{\partial c_\alpha}{\partial x_i} + u_i c_\alpha \right) = R_\alpha \tag{1}$$

where c_α denotes the oxygen concentration, D_α the relevant diffusion coefficient, u_i the gas velocity component in direction i, and R_α the volumetric sink term associated with electrochemical oxygen consumption in the cathode [25,26].

2.1. Through-plane oxygen transport

In the governing species balance from Eq. (1), the diffusive flux term $-D_\alpha \frac{\partial c_\alpha}{\partial x_i}$ captures oxygen transport driven by concentration gradients, while the source/sink term R_α provides the coupling to electrochemical consumption in the catalyst layer. As shown in Fig. 1, oxygen transport along the through-plane pathway from the gas channel to the cathode active sites involves several coupled steps across the GDL/MPL and within the porous catalyst layer. Transport is typically dominated by molecular diffusion across the larger pores of the GDL, may shift toward Knudsen-influenced diffusion in finer MPL/CCL structures, and additionally includes diffusion through thin ionomer and water films covering Pt-catalyst particles within the CCL [10,27].

For a compact first-order description, transport across the porous cathode structure can be represented by an effective diffusivity D_{eff}, which accounts for porosity, tortuosity, and the combined molecular and Knudsen contributions. The corresponding characteristic diffusion time scale scales with the square of the transport length l_b and inversely with D_{eff} [17,22,28]:

$$\tau_{diff} = \frac{{l_b}^2}{D_{eff}} \tag{2}$$

Oxygen transport is driven by the concentration difference between the channel-side interface and the catalyst-layer side of the porous transport path. The relaxation time is mainly governed by the effective transport length and effective diffusivity D_{eff}.

Liquid water introduces a nonlinear and locally nonstationary modification of oxygen transport by blocking pores and reducing the gas-accessible transport volume. This changes the effective porosity, tortuosity, and diffusivity of the porous cathode and can therefore increase the oxygen-transport resistance and shift the relaxation time [29–32].

2.2. Along-the-channel gas transport and conversion

Along the cathode channel, oxygen transport is predominantly governed by convection. For the present first-order interpretation, axial diffusion is assumed to be negligible compared with convection, such that Eq. (1) reduces to a one-dimensional convective balance in the channel [17,22,28]

$$\frac{\partial}{\partial z}\left(u_{ch} c_{O_{2,ch}}\right) = -a_{int} R_{O_2(z)} \tag{3}$$

where z is the channel coordinate, u_{ch} is the cross-section-averaged gas velocity, and a_{int} denotes the interfacial area-to-gas-volume ratio, which links oxygen consumption at the electrode to oxygen depletion in the adjacent gas channel. Here, $R_{O_2(z)}$ denotes the local area-specific oxygen consumption rate at axial position z.

The axial driving force is the cumulative oxygen consumption along the channel, which progressively depletes $c_{O_{2,ch}}$ from inlet to outlet, consistent with the color gradient in Fig. 1. The resulting decrease in oxygen activity lowers the local Nernst potential and increases concentration overpotential, thereby contributing to the along-the-channel distribution of local overpotential under load.

A convenient first-order time scale for channel transport is the convective residence time, which scales with channel length L and inversely with the mean gas velocity in the channel [19,33]:

$$\tau_{ch} = \frac{L}{u_{ch}} \tag{4}$$

The channel-related low-frequency contribution depends on how rapidly oxygen is replenished by convection relative to how rapidly it is consumed electrochemically. It is therefore controlled by gas velocity, oxygen consumption, and coupling to through-plane transport in the porous cathode.

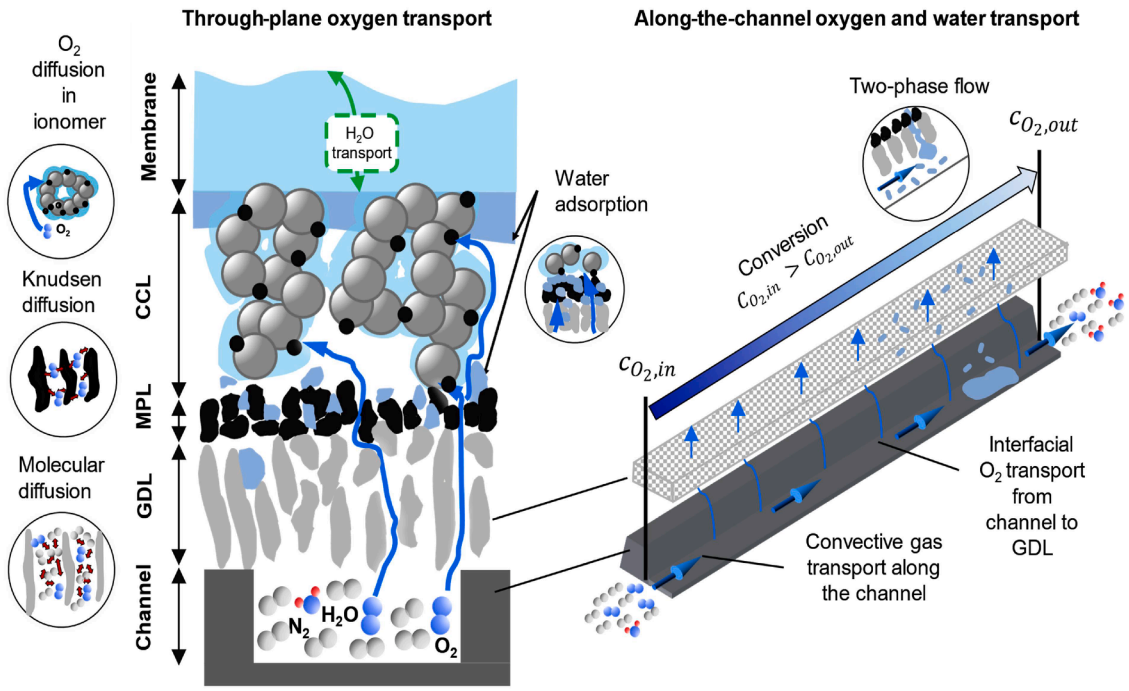

Fig. 1. Schematic overview of coupled oxygen and water transport processes in PEMFC cathodes, including through-plane and along-the-channel pathways.

When convective renewal is strong, axial oxygen gradients remain small, and the channel-related contribution can become weak compared with the local through-plane oxygen-transport contribution. Conversely, at technical stoichiometries and toward the channel outlet, cumulative oxygen consumption can amplify axial depletion and thereby strengthen the channel-related low-frequency response [7,17,33].

2.3. Coupling between convection and diffusion at the channel–electrode interface

The coupling between channel convection and porous-layer transport is established at the channel–GDL interface and may be expressed by an interfacial mass-transfer relation,

$$N_{O_2,ch-GDL} = k_g\left(c_{O_2,ch} - c_{O_2,surf}\right) \tag{5}$$

where $N_{O_2,ch-GDL}$ is the molar oxygen flux from the channel into the GDL, k_g is the gas-side interfacial mass-transfer coefficient, $c_{O_2,ch}$ the channel bulk concentration, and $c_{O_2,surf}$ is the concentration at the channel-side GDL surface.

The coefficient k_g describes the gas-side interfacial mass transfer between the channel bulk and the GDL surface. In reduced PEMFC models, this interfacial transport is commonly parameterized through a Sherwood-type relation, so that k_g depends on the channel flow conditions through the corresponding Sherwood number correlation. Higher gas velocities therefore tend to reduce the external gas-side transport resistance and keep the interfacial concentration $c_{O_2,surf}$ closer to the bulk channel value $c_{O_2,ch}$ [34–36].

Liquid water can affect both sides of this coupling. Within the porous electrode, pore blockage reduces the effective transport coefficient and accessible gas volume, whereas in the channel two-phase flow by films or slugs may thicken the gas-side boundary layer, modifying the local velocity field and thereby reducing the effective interfacial mass transfer [29,36–38].

3. Experimental

All experiments were conducted on a test bench based on the concept for incremental cell measurements [8,15,39], which was adapted and extended for spatially resolved measurements. A photograph of the experimental setup, including the test bench and the custom segmented cell installed and wired for operation, is shown in Fig. 2a.

Fig. 2c,d show the custom segmented cell hardware used in this study, consisting of 13 electrically insulated anode segments and an unsegmented cathode plate. Each anode segment has an active area of 4 cm^2, enabling an approximately homogeneous operating state within each segment and mapping gradients along the cell. Each segment provides individual current, voltage, and temperature sensing. In addition, a force sensor (model 8416, Burster, Gernsbach, Germany) is integrated in each segment, which can be adjusted manually via adjusting screws. This enables a continuous quantification of the locally applied clamping force and a homogeneous compression of the active materials. The sealing around the active area is compressed separately by dedicated screws, decoupling sealing compression from active-area compression.

The anode and cathode flow fields are based on a parallel channel-rib structure with geometries representative for mobile applications [40]. The flow field length is 260 mm, which allows along-the-channel gradients to develop similarly to long straight-channel stack designs [3,4,41]. The flow field width of the cell is 20 mm. Heating cartridges distributed in anode and cathode steel plates are used to adjust the cell temperature.

The cell was operated with a commercial catalyst-coated membrane (CCM) with a total active area of 52 cm^2. A non-segmented gas diffusion layer (GDL) with a microporous layer (MPL) was used on both the anode and cathode sides (H14CX483, Freudenberg, Weinheim, Germany) [42]. This configuration preserves continuous in-plane transport pathways for gas and water and is therefore more representative of real PEMFC stacks. The associated effect on the electrical segmentation of the anode side was considered acceptable in order to retain transport conditions comparable to those in real stack operation.

3.1. Current density distribution and local sequential EIS

Fig. 2b illustrates the measurement setup and the electrical wiring of the cell and demonstrates the measurement principle. Centrally depicted

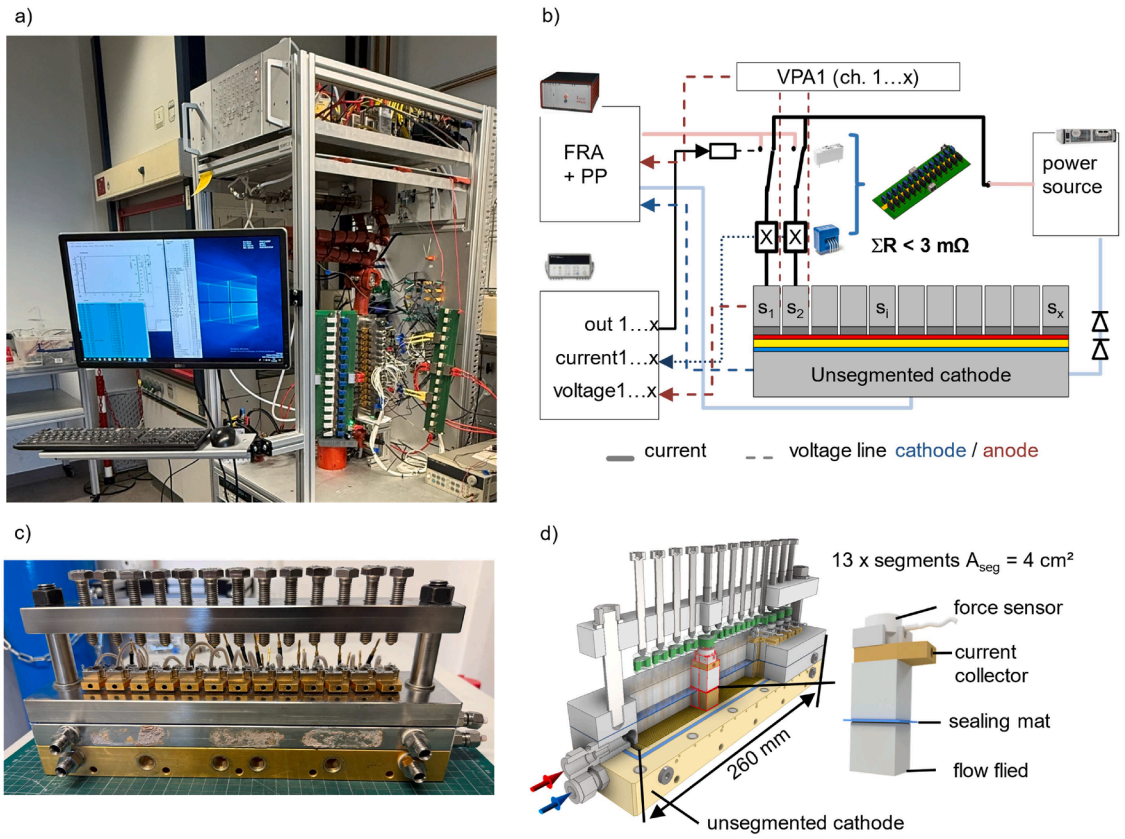

Fig. 2. Segmented cell setup and measurement concept. (a) Photograph of the complete segmented-cell setup mounted and wired at the test bench. (b) Schematic of the measurement principle and electrical wiring of the segmented cell for sequential local EIS measurements. (c) Photograph of the segmented-cell hardware. (d) Segmented cell housing and segment concept.

is the segmented cell with anode-side segmentation from segment S1 to segment S13. Each cell segment can be connected to two circuits for direct current (DC) and alternating current (AC) measurements, enabling current density distribution measurements and EIS measurements for an individual segment.

For current density distribution measurements, a DC power source (N8733A, Keysight Technologies, Santa Rosa, CA, USA) is connected to the cathode side as a common current collector, and to an in-house designed printed circuit board (PCB) (Fig. 2b). From the PCB, the total current is divided into 13 parallel paths, one for each segment. A DC current is galvanostatically applied to the entire cell via the power source. Since only the total current is controlled, both current and voltage of the segments are floating. To achieve conditions similar to a stack with metallic interconnectors, all segments should exhibit the same potential. This is achieved by keeping the resistances between the segments and the common current collector on the PCB similar and very small (here < 3 mΩ). Depending on the local resistances and the total current applied, the current is distributed across the segments. Closed loop Hall sensors (LKSR 15-NP LEM, Meyrin, Switzerland) on the PCB are applied to measure the local currents of each segment. The voltage signal for each segment is recorded individually by a multichannel data logger to ensure that all segments are operated at the same voltage.

A key advantage of the setup is, through a secondary AC path, an AC current and the required DC bias can be applied to a selectable segment. An electrochemical Zahner Zennium workstation (Zahner, Kronach, Germany) equipped with a power potentiostat can be connected automatically to any of the thirteen segments, allowing for sequential EIS measurements on the selected segment. To perform local sequential EIS measurements, the local current of the selected segment is recorded for a given total cell current. The total current specified by the DC current source is reduced by the segment current and then applied via the power potentiostat using the AC path to ensure that the local and overall operating state of the cell remains unchanged. The sinusoidal current perturbation is applied through the electrochemical workstation via the power potentiostat. Low-resistance relays (AZ742–2CG-12DE, Zettler Electronics GmbH, München, Germany) on the PCB switch the individual segments between AC and DC paths. Simultaneously, the voltage of the excited segment is routed to the impedance analyzer.

The segmented PEM fuel cell was operated under stack-relevant conditions in co-flow configuration using humidified hydrogen (anode) and humidified synthetic air (cathode). The cathode feed contained 21 vol% O_2 on a dry basis (balance N_2). Under humidified operation the oxygen partial pressure is therefore reduced by the water vapour partial pressure. Unless stated otherwise, the standard conditions were 100 kPa backpressure (overpressure) and stoichiometries of 2.0 on both the anode and the cathode. For the inter-gas variation, the cathode feed was switched from O_2/N_2 to O_2/He at identical oxygen partial pressure and identical cathode stoichiometry, so that the channel velocity remained unchanged while the gas-phase oxygen diffusivity was varied.

The compression was adjusted to 1 MPa to ensure homogeneous GDL compression and reliable electrical contacting. It should be noted that such locally verified homogeneous compression is difficult to achieve in technical stacks. Because the clamping force applied to the end plates is distributed over both the active area and the sealing, even small component height tolerances may result in locally inhomogeneous compression.

To mimic stack-relevant operation, the overall cell current was applied galvanostatically, while the local segment currents distribute according to the local electrochemical state. Each current density was held for 20 min to ensure steady-state conditions before recording the current-density distribution. Subsequently, local EIS spectra were

acquired sequentially along the channel from outlet to inlet for selected segments (13,10,7,4,1) to map spatial shifts in electrochemical processes. This acquisition order minimizes the risk of perturbing the gas composition or water state of downstream segments before their measurement.

For each local EIS measurement, the entire cell was first set to a current-free state before the selected segment was relay-switched from the DC path to the AC path. The relay switching time was below 10 ms, and a waiting time of 10 s was applied before the local segment current was imposed again through the AC path. The operating point was sustained for another 30 min before impedance acquisition.

The cell and current-distribution electronics were operated electrically floating, while only the Zahner impedance analyzer was connected to ground. Impedance spectra were recorded from 0.1 Hz to 100 kHz with 11 points per decade below 66 Hz and 6 points per decade above 66 Hz. The signal was integrated over 20 periods at each frequency point. The perturbation amplitude was set to 15% of the local segment current, resulting in a segment voltage response amplitude of $\leq$ 20 mV to ensure small-signal linearity. Signal linearity was further verified by monitoring the voltage response during the measurements. Measurements were repeated to identify non-stationary behavior and to confirm the reproducibility of the low-frequency response, including under high-flow operating conditions.

The validity of the impedance data was verified using the Kramers–Kronig test [43]. The residual error for all spectra remained below 2%, indicating high data quality and supporting the reliability of the low-frequency data. To deconvolute electrochemical processes and their characteristic time constants, each local impedance spectrum was analyzed using the distribution of relaxation times (DRT) [8,44]. DRT calculations are based on Tikhonov regularization [45]. For all DRT analyses, a carefully chosen regularization factor of 0.005 was used.

4. Results and discussion

Initially, a representative local impedance spectrum is analyzed to introduce the characteristic features of the local response. This is followed by a sensitivity analysis at the inlet segment, which serves as the reference for the subsequent along-the-channel analysis.

4.1. Analysis of a local impedance spectrum

Fig. 3a shows a representative local impedance spectrum extracted from the segmented cell dataset under standard operating conditions at $j_{cell,mean} = 0.5$ A cm^{-2}. Segment 1 is taken as a representative example to introduce the characteristic peaks and the subsequent DRT-based conclusions. The same qualitative peaks are observed for all segments. Their along-the-channel evolution is discussed later. The impedance spectrum exhibits a pronounced high-frequency semicircle and an additional low-frequency response with two discernible arcs. Consistently, the Kramers–Kronig residuals in Fig. 3b increase at the highest frequencies, whereas the residuals remain within ±1% over the frequency range relevant to the present analysis, confirming that the low-frequency peaks are not artifacts of poor data quality.

To deconvolute the overlapping polarization contributions, Fig. 3c shows the DRT g(f), resolving five distinct peaks with characteristic frequencies of approximately 3.8 Hz (P_{LF1}), 17.7 Hz (P_{LF2}), 120 Hz (P_{MF}), 0.8 kHz (P_{HF1}), and 8.1 kHz (P_{HF2}). For the mid- and high-frequency range, peak assignment was established by systematic operating-condition variations following the parameter-dependency logic introduced by Heinzmann et al. [8]. The results are consistent with prior DRT studies [8,46,47]. P_{HF1} and P_{HF2} are attributed to proton/ionic transport in the membrane/ionomer phase [48], while P_{MF} is assigned to the cathode charge-transfer (ORR) process in the catalyst layer. The much smaller anode processes of this type of CCM are located in the same frequency range [8].

Most PEMFC DRT studies report one dominant low-frequency peak,

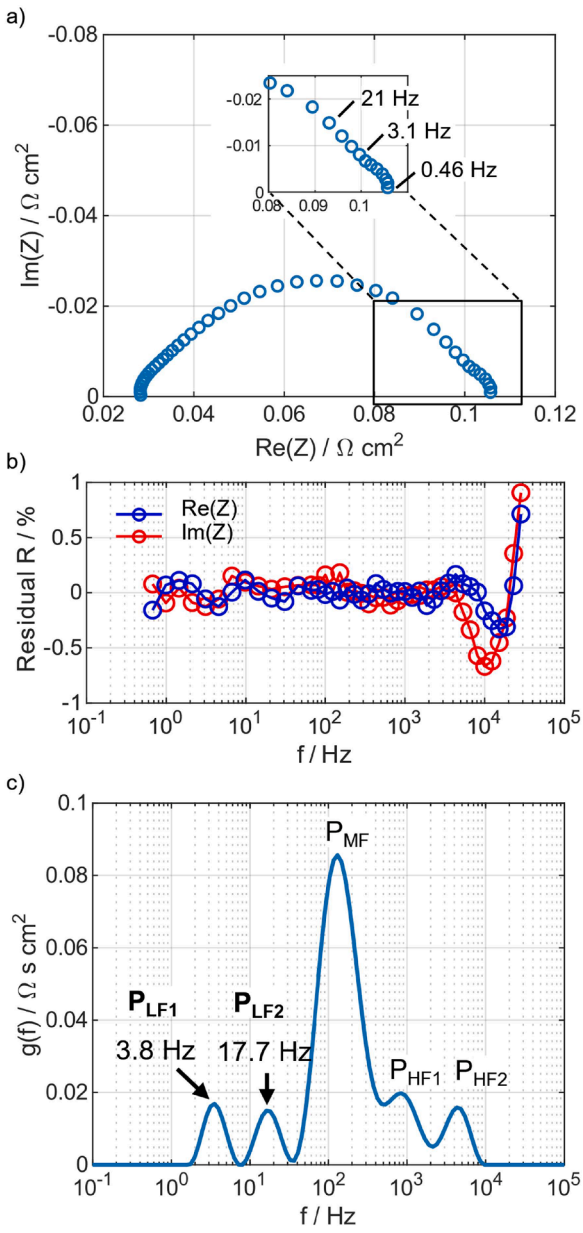

Fig. 3. (a) Nyquist plot of the measured EIS at the gas inlet (Segment 1) under standard conditions at $j_{cell,mean} = 0.5$ A cm^{-2} with a zoom into the low-frequency. (b) Corresponding Kramers-Kronig residuals and (c) distribution of relaxation times with designation to different polarization processes.

typically located in the range of approximately 2–20 Hz and commonly assigned to oxygen transport limitations in the porous cathode [8,39,49]. However, several studies indicate that this low-frequency response can contain more than one transport contribution. For example, the lowest-frequency DRT peak may represent merged oxygen-transport contributions from both the GDL and the gas channel [9]. Additional low-frequency peaks have also been observed at lower cell voltages or in cathode-outlet regions of spatially resolved PEMFC measurements, although their assignment is not always unambiguous [3,50]. Recent work further reported two low-frequency mass-transport peaks, with the lower-frequency contribution linked to flow-field-related losses [51].

This interpretation is also supported by the more general distinction between diffusion and gas-conversion impedances known from SOFC analysis. In these systems, low-frequency concentration losses can be separated into diffusion through the porous support and conversion related to the gas volume and reactant consumption [52,53]

Transferred to the PEMFC cathode, this suggests that channel-scale and porous-electrode oxygen transport can also appear as separate low-frequency contributions when their characteristic time scales differ sufficiently.

A channel-related low-frequency process is then expected to depend primarily on convective residence time, axial oxygen depletion due to electrochemical consumption, and the strength of gas-side coupling between channel convection and porous-electrode transport at the channel–GDL interface. Its characteristic time scale and amplitude should therefore vary mainly with gas velocity or stoichiometry, overall oxygen consumption, and the interfacial mass-transfer coefficient governing this coupling. Under wet operating conditions, these dependencies may be further modified by two-phase flow in the channel, for example through water films or slugs that alter local flow distribution and gas-side mass transfer[7,16,20,28,33].

By contrast, a through-plane oxygen-transport process is expected to depend primarily on the local oxygen flux from the channel toward the catalyst layer, driven by the local concentration gradient and governed by the effective diffusivity and transport path length within the porous cathode structure. It should therefore be particularly sensitive to current density, local oxygen availability, water state, and water-dependent changes in oxygen transport within the GDL, MPL, and CCL [8,10, 29–32].

4.2. Sensitivity analysisof LF processesat the inletsegment

To assign P_{LF1} and P_{LF2} to their underlying physical origin, the sensitivities of both low-frequency peak are examined by means of targeted parameter variations. For this purpose, inert-gas, cathode-stoichiometry, current-density, and relative-humidity variations are carried out under otherwise standard operating conditions using the full segmented cell.

As local operating conditions evolve continuously along the channel, trends extracted from all segments simultaneously may be difficult to interpret unambiguously. The analysis therefore begins with the inlet segment (Segment 1) as a reference case. At this position, gas composition, humidity, stoichiometry, local current density, and channel velocity are most clearly defined and least affected by upstream reactant conversion and water accumulation. This provides the most controlled basis for assessing the sensitivities of P_{LF1} and P_{LF2} before extending the interpretation to the full along-the-channel behavior in the next section.

4.3. Inert-gas variation

By replacing N_2 with He, the effective oxygen diffusivity in the cathode gas mixture is increased while oxygen partial pressure and gas velocity remain unchanged. The type of inert gas furthermore does not affect charge transfer or ionomer transport processes directly. There

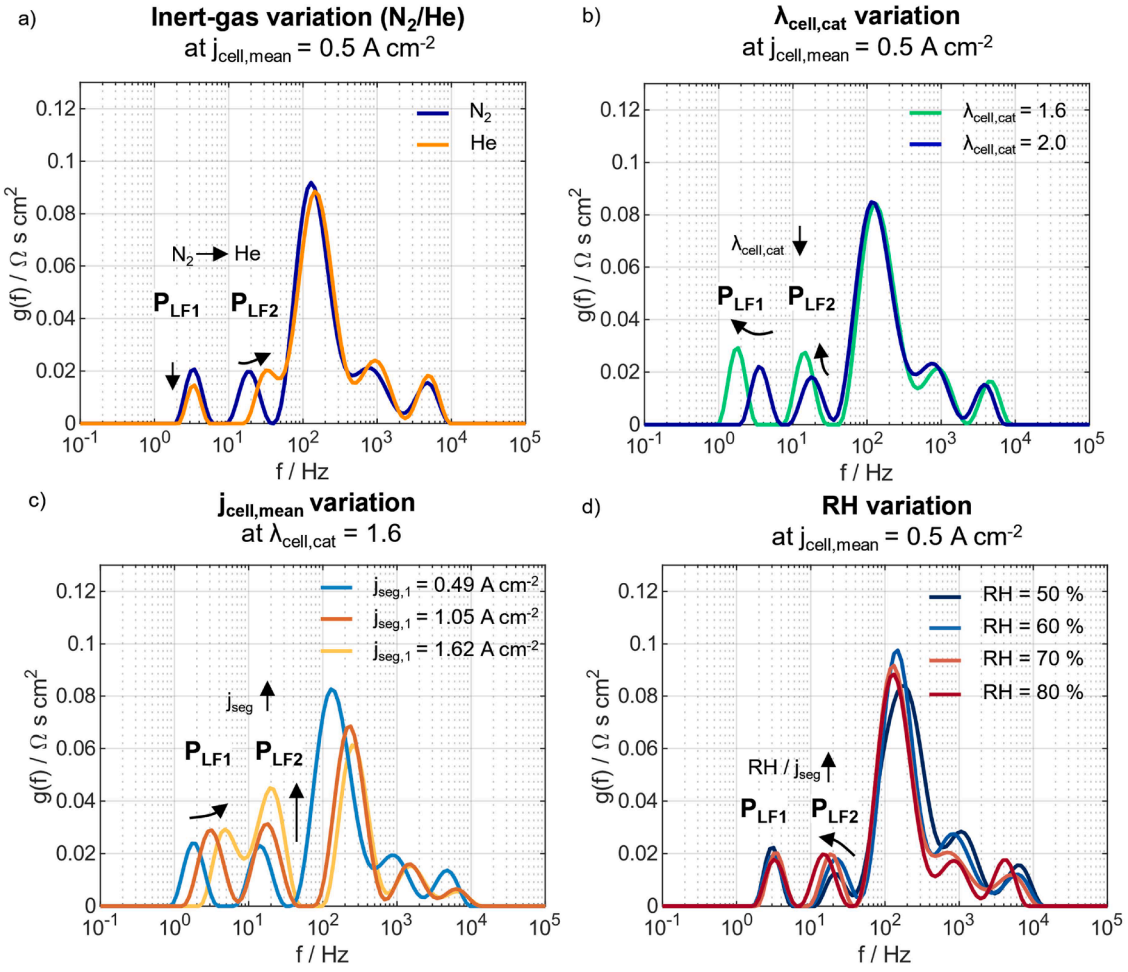

Fig. 4. DRT of Segment 1 highlighting the two low-frequency peaks P_{LF1} and P_{LF2} for four targeted parameter variations. (a) Cathode inert-gas variation from N_2 to He at constant p_{O2}, u_{ch}, and nearly constant local current density, yielding $j_{seg,1}$ = 0.40 and 0.385 A cm^{-2} for N_2 and He, respectively. (b) Cathode stoichiometry variation, $\lambda_{cell,c}$ = 1.6 and 2.0, at $j_{cell,mean}$ = 0.5 A cm^{-2}, yielding $j_{seg,1}$ = 0.49 and 0.44 A cm^{-2}, respectively. (c) Mean cell current-density variation, $j_{cell,mean}$ = 0.5, 1.0, and 1.5 A cm^{-2}, at $\lambda_{cell,c}$ = 1.6, yielding $j_{seg,1}$ = 0.49, 1.05, and 1.62 A cm^{-2}, respectively. (d) Cathode relative-humidity variation, RH = 50, 60, 70, and 80%, at $j_{cell,mean}$ = 0.5 A cm^{-2}, yielding $j_{seg,1}$ = 0.33, 0.38, 0.40, and 0.46 A cm^{-2}, respectively. Arrows indicate the direction of the shifts in P_{LF1} and P_{LF2}.

might be some impact if the local gas composition and humidity in the CCL are affected by the different diffusivities. The inert gas variation therefore primarily probes the sensitivity of the low-frequency peaks to diffusive oxygen transport in the gas phase. As shown in Fig. 4a, P_{LF2} exhibits the clearest response to the inert-gas substitution by shifting toward higher frequencies with increasing effective oxygen diffusivity. This behavior is consistent with the trend expected from Eq. (2) for a diffusion-related transport process [8,20]. Additionally, Eq. (2) allows an order-of-magnitude estimate of the effective oxygen diffusivity from the P_{LF2} peak frequency. Using $l_b = 140$ µm [42] the resulting values are $D_{eff} \approx 2.2\,10^{-6}\,m^2\,s^{-1}$ at 17.7 Hz for O_2/N_2 and $D_{eff} \approx 3.9\,10^{-6}\,m^2\,s^{-1}$ at 31.7 Hz for O_2/He. These values lie in a plausible range and are consistent with effective oxygen diffusivities reported in the literature [9,17], supporting the interpretation of P_{LF2} as a through-plane oxygen-transport process.

In contrast, P_{LF1} shows essentially no change in characteristic frequency upon the N_2/He substitution. This invariance argues against a time constant primarily controlled by oxygen diffusivity and instead points to a process whose dominant time scale is largely independent of the molecular diffusivity in the gas mixture. Since the channel gas velocity is kept constant, this behavior is consistent with the flow-rate-dependent scaling expected from Eq. (3).

A direct back-calculation of a characteristic length scale from the P_{LF1} frequency was not pursued, because under sequential segment-wise EIS the local perturbation is imposed only on a single segment and the corresponding gas-phase response cannot be mapped unambiguously onto a single geometric channel length.

Changes in amplitude cannot be assessed unambiguously for P_{LF2} because the high oxygen excess at the inlet limits the overall transport resistance and, in addition, partial overlap of P_{LF2} with adjacent charge transfer contributions P_{MF} in the He case prohibits a quantitative comparison. The amplitude of P_{LF1} likewise changes only weakly. Any minor residual sensitivity may therefore be attributed to a secondary coupling via gas-side interfacial mass transfer at the channel–GDL interface, as described by Eq. (5), rather than to direct diffusive control of the process itself.

4.4. Cathode stoichiometry variation

A reduction in cathode stoichiometry decreases both the oxygen excess and the cathode gas flow rate, and therefore also lowers the channel gas velocity, u_{ch}. While the inlet oxygen mole fraction remains unchanged, the reduced stoichiometry weakens convective oxygen renewal and promotes a stronger oxygen depletion along the cathode channel under load. Stoichiometry variation is therefore expected to affect both a channel-related process, through the change in gas velocity and axial oxygen depletion, and a through-plane oxygen-transport process, through the reduced local oxygen availability.

As shown in Fig. 4b, both P_{LF1} and P_{LF2} respond to the stoichiometry variation by shifting to lower frequencies and by increasing in amplitude. At lower oxygen availability, sustaining the same reaction rate requires a larger concentration gradient between the channel and the catalyst layer to maintain the required oxygen flux. This increases the effective oxygen transport resistance, which can appear as an increased amplitude of the corresponding transport peak and may shift the associated relaxation process toward lower frequencies [10,17]. The P_{LF1} frequency increases with increasing cathode stoichiometry, consistent with the trend expected for a gas-velocity-related process. However, the measured frequency shift is larger than predicted by simple residence-time scaling according to Eq. (3). This indicates that P_{LF1} is influenced not only by channel convection but also by oxygen depletion and channel–electrode coupling [17–19]. The increase in P_{LF1} amplitude, despite nearly identical local current density at the inlet segment, further supports this coupled interpretation.

4.5. Current density variation

Under stoichiometric operation, an increase in overall cell load is accompanied by a proportional increase in cathode gas flow rate and thus in channel gas velocity, u_{ch}. At the same time, depending on the local resistance distribution, the local current density also increases. Fig. 4c shows the corresponding changes in the DRT for Segment 1. The two low-frequency peaks exhibit clearly different sensitivities to the imposed load variation. P_{LF2} increases markedly in amplitude, while its characteristic frequency remains nearly unchanged. By contrast, P_{LF1} shifts to higher frequencies, whereas its amplitude increases only slightly. The higher current density increases the oxygen demand at the cathode catalyst layer and therefore the required oxygen flux from the channel to the reaction sites. This explains the increase in P_{LF2} amplitude with increasing load [8,10]. Since the effective diffusivity is not directly changed and no strong additional liquid-water effect is expected at the inlet, Eq. (2) does not predict a pronounced P_{LF2} frequency shift [8,28].

In contrast, the observed P_{LF1} frequency shift scales approximately with the increase in u_{ch} and is therefore consistent with the trend expected from Eq. (3) for a flow-related process. Small changes in P_{LF1} amplitude may indicate an additional coupling contribution, but cannot be assessed unambiguously because at high current density the characteristic time scales of P_{LF1} and P_{LF2} begin to overlap partially. At sufficiently high u_{ch}, an increasing overlap or even merging of both peaks can be expected, as the channel-related contribution becomes less distinct relative to the through-plane oxygen-transport process [19,28]. This tendency is further supported by the current-density variation at Segment 1 under constant high gas flow, as shown in the supplementary material (Fig. S1).

4.6. Relative humidity variation

By increasing cathode RH, the water-vapor fraction in the gas mixture increases while the oxygen fraction decreases slightly. In principle, the additional water vapor also causes a slight increase in the total gas volumetric flow rate and thus in the channel gas velocity, u_{ch}. Under the present operating conditions, however, this increase is negligibly small and can be neglected to first order. Improved hydration lowers the local ionic resistance [8,41] and increases the local current density.

As shown in Fig. 4d, P_{LF2} shows the strongest response to the RH variation. With increasing RH, P_{LF2} slightly increases in amplitude and shifts to lower frequencies. Improved ionomer hydration alone would be expected to reduce thin-film oxygen-transport resistance. In the present case, however, the simultaneous increase in local current density appears to dominate, increasing the local oxygen demand [10]. In addition, the lower oxygen fraction and higher water content can further hinder oxygen transport in the porous cathode. These effects explain the observed P_{LF2} shift toward lower frequencies according to Eq. (2). By contrast, P_{LF1} remains essentially unchanged in frequency, and no systematic amplitude trend is observed. Since the RH-induced change in u_{ch}. is negligible under the present conditions, this supports the interpretation of P_{LF1} as a predominantly channel-related process [19].

4.7. Along the channel analysis

The sensitivities identified at Segment 1 are now transferred to the along-the-channel behavior under technically relevant operating conditions. This allows the effects of oxygen consumption and water accumulation along the cathode channel to be assessed directly. The evolution of P_{LF1} and P_{LF2} is analyzed for current-density, inert-gas, cathode-stoichiometry, and relative-humidity variations at Segments 1, 4, 7, 10, and 13. The corresponding along-the-channel profiles of the ohmic resistance Rohm and polarization resistance R_{pol} are provided in the Supplementary Material (Fig. S 2–5).

4.7.1. Along the channel current density variation

At $j_{cell,mean}$ = 0.5 A cm^{-2}, the along-the-channel current-density distribution remains comparatively homogeneous, showing only a slight increase from the inlet toward the cell center and a moderate decrease toward the outlet as seen in Fig. 5a. This suggests that local conditions remain relatively balanced at low load, with the most favorable combination of oxygen availability and hydration state in the middle segments 4 to 10. This interpretation is consistent with the corresponding R_0 and R_{pol} distributions in Fig. S2.

These trends are reflected in the low-frequency transport contributions shown in Fig. 5b – c. P_{LF2} amplitude is lowest in the middle of the cathode flow path, although the local current density is slightly higher there. This indicates more favorable local oxygen-transport conditions, most likely due to improved hydration. At the inlet, P_{LF2} is larger despite the lower local current density and high oxygen availability. This is consistent with comparatively dry local conditions, as indicated by the elevated R_0, which can increase the ionomer-related contribution to through-plane oxygen transport in the porous cathode. Toward the outlet, P_{LF2} increases again because oxygen is progressively depleted by upstream consumption and water accumulation in the porous cathode becomes more likely. The P_{LF2} frequency follows the same non-monotonic behavior. It increases from the inlet toward the cell center and decreases again toward the outlet. Thus, the effective oxygen-transport response is fastest under the more favorable mid-channel conditions and becomes slower toward both inlet and outlet.

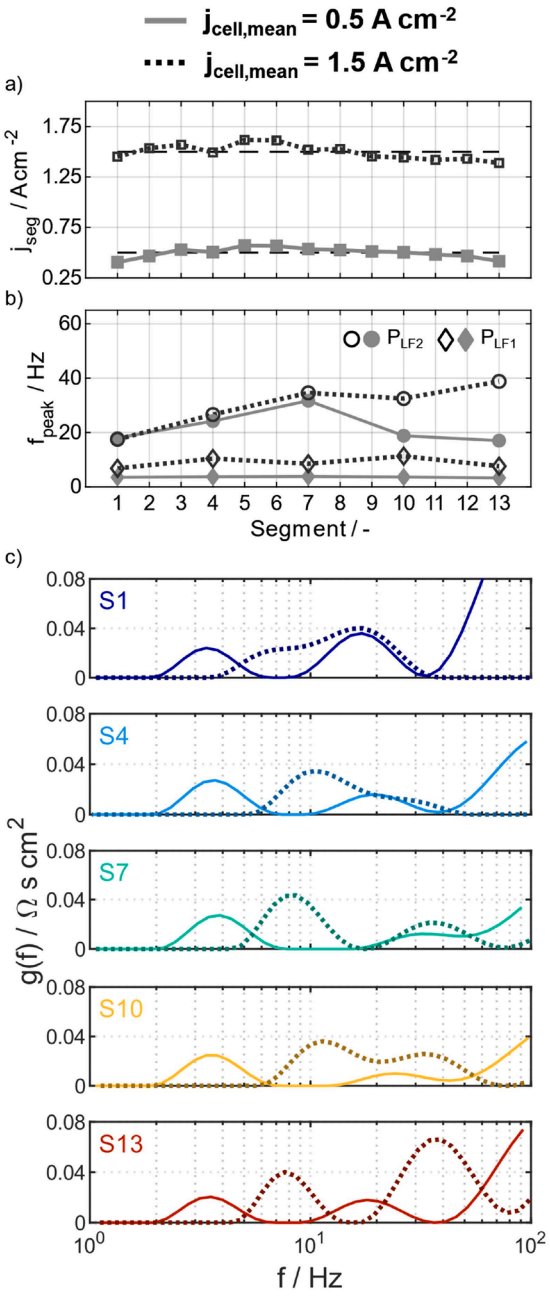

Fig. 5. Along-the-channel distributions of (a) local current density, (b) peak frequencies of P_{LF1} and P_{LF2}, and (c) low-frequency DRT contributions for mean cell current densities of 0.5 and 1.5 A cm^{-2} under standard operating conditions. The lower panels show selected segments (S1, S4, S7, S10, and S13). Solid lines denote 0.5 A cm^{-2} and dotted lines 1.5 A cm^{-2}.

In contrast, P_{LF1} remains nearly constant along the channel at $j_{cell,mean}$ = 0.5 A cm^{-2}, and its amplitude shows no systematic trend. At low load, axial oxygen depletion is weak, so the channel-related contribution changes only slightly along the flow field. The nearly constant P_{LF1} frequency is also consistent with an approximately constant mean channel gas velocity from inlet to outlet. Although oxygen consumption and water transport can locally modify the molar gas flux, these effects appear to compensate to first order under the present low-load conditions. The absence of pronounced outlet amplification further indicates that severe liquid-water blockage is not dominant in this case.

When the mean current density is increased to $j_{cell,mean}$ = 1.5 A cm^{-2}, reactant consumption and water production both increase, resulting in more pronounced along-the-channel gradients. Fig. 5a shows a stronger current-density decrease from the cell center toward the outlet than in the low-load case.

Accordingly, local through-plane oxygen-transport limitations and channel-related effects become more pronounced, as reflected by the increased low-frequency contributions in Fig. 5b.

The strongest change is observed for P_{LF2} near the outlet. Its amplitude increases much more strongly than at 0.5 A cm^{-2}, indicating a more severe downstream oxygen-transport limitation caused by enhanced oxygen depletion and increased water accumulation in the porous cathode layers [9,10]. At the same time, the frequency trend changes compared with the low-load case. At 0.5 A cm^{-2}, the outlet region shows a slower P_{LF2} response. At 1.5 A cm^{-2}, P_{LF2} remains large but shifts to higher frequencies. This indicates that the high-load outlet response is not governed by oxygen depletion alone. Water-related changes in the porous cathode must also contribute.

Oxygen depletion alone would be expected to increase the local oxygen-transport resistance and shift P_{LF2} to lower frequencies. However, liquid-water accumulation can reduce the gas-filled pore volume, modify the effective transport path, and decrease the oxygen storage capacity of the remaining gas-filled domain. These effects may accelerate the apparent local concentration response and shift P_{LF2} to higher frequencies. Stronger self-humidification at high load, reflected by the reduced R_0, may further contribute through improved membrane and ionomer hydration [10,27]. In addition, because the cathode stoichiometry is kept constant at $\lambda_{cell,cat}$ = 2 with respect to the full cell, the inlet flow rate and channel gas velocity increase with current density. This can support water removal and partly delay severe two-phase blockage. Overall, the high-load outlet behavior of P_{LF2} therefore reflects competing effects of oxygen depletion, water accumulation, local oxygen storage, and improved hydration.

At $j_{cell,mean}$ = 1.5 A cm^{-2}, P_{LF1} shifts to higher frequencies and moves closer to P_{LF2}, which promotes partial overlap, especially near the inlet. Along the channel, the P_{LF1} frequency lies roughly between 7 and 13 Hz and does not show a clear monotonic trend. This suggests that the simple assumption of an approximately constant u_{ch} becomes less valid at high load. Instead, the local P_{LF1} frequency appears to be affected by spatial variations in the channel, most likely caused by stronger water accumulation and evolving two-phase effects [10]. The P_{LF1} amplitude increases toward the outlet at high load. This is consistent with cumulative oxygen consumption along the cathode channel and the resulting progressive oxygen depletion from inlet to outlet. The stronger axial

depletion also enhances the coupling between channel oxygen transport and local through-plane oxygen transport through the porous cathode, as described by the interfacial mass-transfer relation in Eq. (5). Under high-load outlet conditions, this coupling may be further intensified when two-phase effects modify the local flow field and reduce the effective gas-side mass-transfer coefficient [10,16,18].

4.7.2. Along the channel inert gas variation

A change in the inert gas from N_2 to He increases the gas-phase oxygen and water-vapor diffusion coefficients, and can therefore help identify oxygen-transport contributions that limit cell performance. Since these effects are expected to be most pronounced at high load, the along-the-channel behavior at $j_{cell,mean} = 1.5$ A cm^{-2} is compared for N_2- and He-based cathode gas mixtures under the standard operating conditions defined in the experimental section.

At identical overall load and inlet conditions, replacing N_2 with He increases the cell voltage by 15 mV, reflecting reduced polarization losses. The resulting redistribution of the local current density along the channel is shown in Fig. 6a. With He, the current density is slightly lower near the inlet but higher from positions midway along the cathode flow path toward the outlet. This indicates that the downstream transport limitation is alleviated under the higher-diffusivity He-containing gas mixture, allowing a larger fraction of the total current to be sustained in the latter part of the channel.

These changes are reflected clearly in the low-frequency contributions shown in Fig. 6b - c. In particular, P_{LF2} decreases markedly in amplitude under He over almost the entire channel, confirming its strong sensitivity to gas-phase oxygen diffusion. At the same time, the characteristic frequency of P_{LF2} shifts to higher values and becomes more uniform along the channel. Compared with the N2 case, this indicates that the along-the-channel non-uniformity of the local through-plane oxygen-transport limitation in the porous cathode layers is reduced when oxygen transport in the gas mixture is facilitated. The reduction in P_{LF2} is most pronounced near the inlet and outlet, whereas it is smaller midway along the cathode flow path. This suggests that the local through-plane oxygen-transport limitation midway along the cathode flow path is less strongly governed by gas-phase diffusion alone. In contrast, the contribution of gas-phase oxygen transport becomes more pronounced toward the inlet and outlet, especially toward the outlet where oxygen depletion and water accumulation are most severe. Under these downstream conditions, the improved gas-phase transport in He partly compensates for both reduced oxygen availability and water-related transport limitations, thereby lowering the P_{LF2} contribution and shifting it to higher frequencies. Because He also increases the gas-phase diffusion coefficient of water vapor, part of this effect may additionally result from enhanced vapor-phase water removal, which can reduce liquid-water accumulation in the porous cathode and near the channel interface and thereby mitigate local two-phase heterogeneity.

At the same time, the He variation also helps to separate the gas-phase-related contribution within P_{LF1} more clearly. While the characteristic frequency of P_{LF1} remains close to that observed under N_2 and no longer shows pronounced along-the-channel fluctuations, its amplitude is only slightly reduced under He near the inlet and becomes progressively more reduced toward the outlet. This is also consistent with the possibility that He promotes vapor-phase water removal and thereby reduces liquid-water-induced flow non-uniformities, especially toward the outlet. This indicates that P_{LF1} is not a purely channel-conversion-controlled peak. Instead, the He sensitivity supports a coupled channel-related origin in which oxygen consumption along the channel is superimposed with gas-phase transport effects and with the coupling between oxygen transport along the channel and local through-plane oxygen transport through the porous cathode layers via interfacial mass transfer at the channel-GDL interface, as described by Eq. (5). The reduced variation of both P_{LF1} and P_{LF2} under He therefore supports the view that part of the strong along-the-channel heterogeneity observed with N_2 arises from gas-phase transport limitations and their coupling to local through-plane oxygen transport in the porous cathode [16,18].

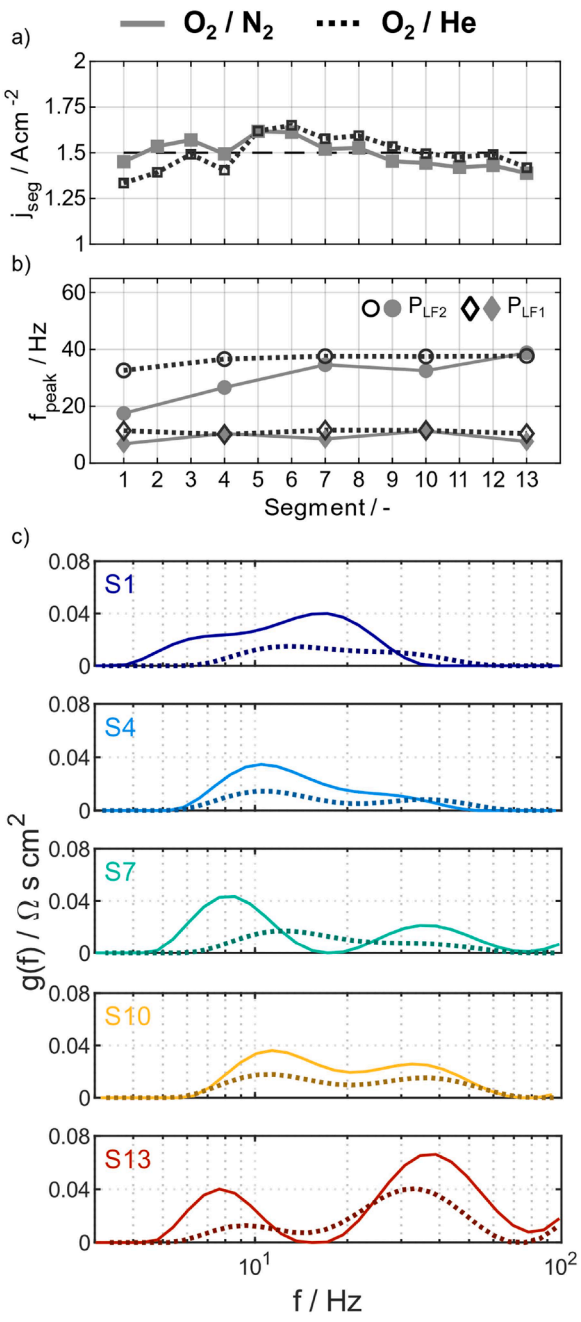

Fig. 6. Along-the-channel distributions of (a) local current density, (b) peak frequencies of P_{LF1} and P_{LF2}, and (c) low-frequency DRT contributions at a mean cell current density of 1.5 A cm^{-2} under standard operating conditions for the reference cathode feed and the He-substituted cathode feed. Solid lines denote N_2 and dotted lines denote He.

4.7.3. Along the channel cathode stoichiometry variation

Reducing the cathode stoichiometry lowers the oxygen excess and thereby increases the oxygen-concentration gradient along the channel at constant mean cell current density. Since stable low-frequency measurements at higher current density were not feasible under these conditions, the analysis is restricted here to $j_{cell,mean} = 0.5$ A cm^{-2}.

As shown in Fig. 7a, the reduced cathode stoichiometry already modifies the local current-density distribution at low load. The current shifts toward the inlet and decreases earlier toward the outlet. This

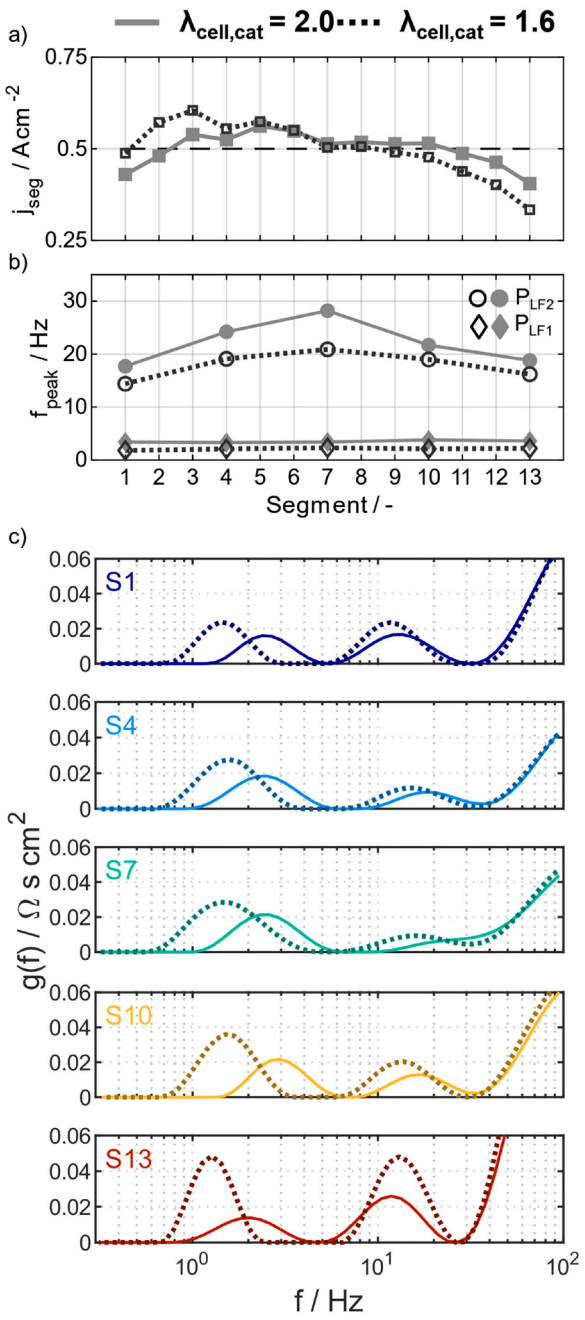

Fig. 7. Along-the-channel distributions of (a) local current density, (b) peak frequencies of P_{LF1} and P_{LF2}, and (c) low-frequency DRT contributions for cathode stoichiometries of 2.0 and 1.6 at a mean cell current density of 0.5 A cm^{-2} under otherwise standard operating conditions. Solid lines denote cathode stoichiometry 2.0 and dotted lines cathode stoichiometry 1.6.

indicates that the along-the-channel transport limitation becomes more pronounced at lower cathode stoichiometry [17].

The low-frequency DRT contributions in Fig. 7b,c show pronounced changes in both P_{LF1} and P_{LF2}. At lower cathode stoichiometry, both peaks shift to lower frequencies along the channel. For P_{LF2}, reduced convective oxygen renewal and stronger oxygen depletion require a larger concentration gradient to sustain the local oxygen flux. This slows the effective through-plane oxygen-transport response. At the same time, the P_{LF2} magnitude increases strongly toward the outlet, especially at Segment 13. This reflects the enhanced downstream oxygen limitation and explains the steeper current-density decay in the second half of the channel. Compared with the reference case at cathode stoichiometry 2.0, the mid-channel optimum becomes less pronounced, while the outlet behavior is increasingly dominated by oxygen-transport limitation.

Importantly, P_{LF1} is also affected by the reduced oxygen excess. Its characteristic frequency decreases at lower stoichiometry, in agreement with the reduced channel gas velocity, while its amplitude increases toward the outlet. This shows that P_{LF1} is not governed by flow rate alone. Instead, these results indicate that local oxygen availability and the coupling between oxygen transport along the channel and local through-plane oxygen diffusion through the porous cathode layers also contribute to the P_{LF1} response [17,18].

4.7.4. *Along the channel relative humidity variation*

Water transport through the membrane affects membrane and ionomer hydration and therefore both ohmic resistance and local oxygen-transport conditions in the cathode [8,10]. Since the water distribution evolves along the channel, it also modifies the spatial distribution of electrochemical activity. To separate these hydration effects from severe two-phase flow effects, wet and comparatively dry cathode conditions are compared at 80% and 50% RH, respectively, at $j_{cell,mean} = 0.5$ A cm^{-2}.

Fig. 8a shows that the humidity variation strongly changes the local current-density distribution. Under dry cathode conditions, the local current density is markedly suppressed near the inlet, increases progressively toward the mid- and downstream region, and decreases again only at the last segments. Under wet conditions, in contrast, the current-density distribution remains much more homogeneous, with only a slight increase from the inlet toward the cell center followed by a moderate decrease toward the outlet. This shows that dry inlet conditions shift electrochemical activity downstream, where product-water formation progressively improves local hydration.

This redistribution is reflected directly in the P_{LF2} behavior (see Fig. 8b – c). Under dry conditions, P_{LF2} is smaller and shifted to higher frequencies in the inlet and mid-channel region. In this region, the strongly reduced local current density lowers the local oxygen demand. At the same time, less liquid-water-induced blockage leaves more gas-filled pore space available for oxygen transport through the porous cathode layers [10]. These effects dominate the observed response despite the reduced oxygen permeability of the less-hydrated ionomer phase, so that P_{LF2} appears smaller and faster. Toward the outlet, however, the trend reverses. As self-humidification restores membrane and ionomer hydration, the local current density rises again in a region where the oxygen concentration has already been reduced by upstream consumption. The resulting increase in local oxygen-flux demand and concentration gradient causes P_{LF2} to grow in amplitude and shift back to lower frequencies. Under dry operation, P_{LF2} therefore changes from a relatively weak and fast response near the inlet to a stronger and slower response toward the outlet.

Under wet conditions, P_{LF2} is already more pronounced at the inlet, decreases toward the mid-channel region, and increases again toward the outlet. This non-monotonic behavior follows the local current-density distribution and shows that P_{LF2} is governed by two coupled factors: local oxygen demand and the severity of the local through-plane oxygen-transport limitation in the porous cathode layers [8]. Thus, the P_{LF2} response is not determined by hydration alone. The effect of water must be distinguished by transport domain. Increased hydration of the ionomer phase can improve oxygen transport within hydrated ionomer regions. In contrast, liquid-water accumulation in the pore space reduces the gas-accessible transport domain and restricts oxygen transport through the gas-filled pore network of the porous cathode layers. Near the inlet, better ionomer hydration is beneficial. However, this benefit is outweighed by the higher local current density and the resulting increase in required oxygen flux. Therefore, P_{LF2} appears larger despite locally improved ionomer-related transport properties. In the cell center, favorable ionomer hydration and still comparatively high oxygen availability reduce the local through-plane oxygen-transport limitation.

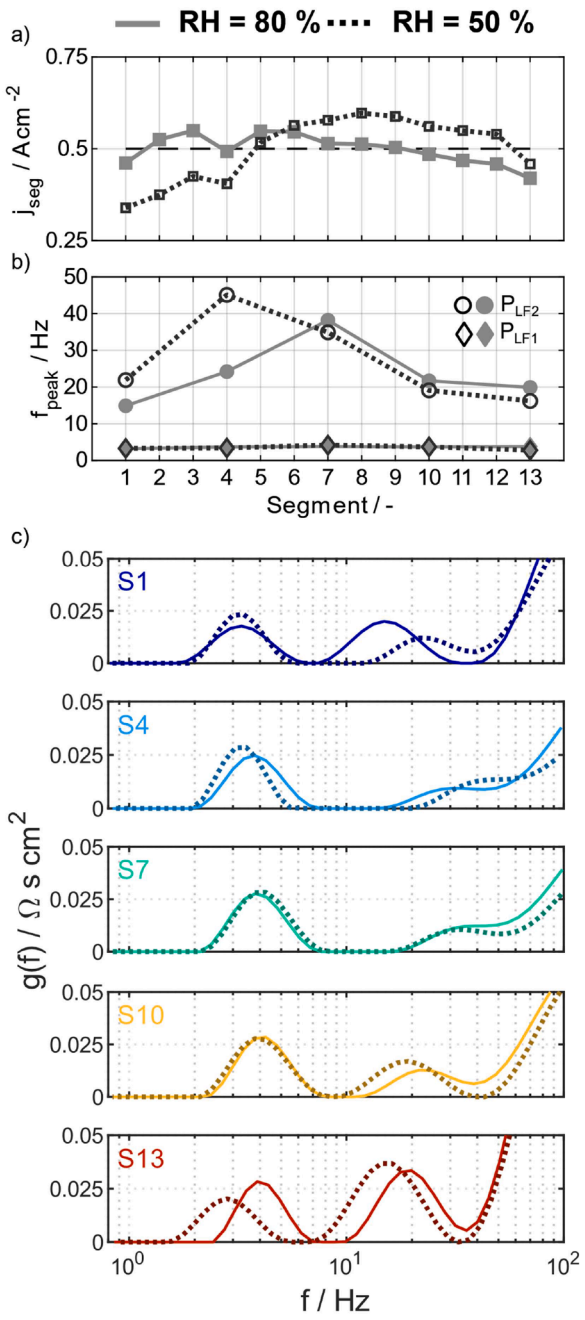

Fig. 8. Along-the-channel distributions of (a) local current density, (b) peak frequencies of P_{LF1} and P_{LF2}, and (c) low-frequency DRT contributions for cathode relative humidities of 80 and 50% at a mean cell current density of 0.5 A cm^{-2} under otherwise standard operating conditions. Solid lines denote RH = 80 %, and dotted lines denote RH = 50 %.

Toward the outlet, oxygen depletion and increasing liquid-water accumulation in the porous structure dominate again. This leads to a stronger oxygen-transport limitation in the porous cathode layers. Compared with the wet case, dry operation suppresses the upstream contribution and progressively shifts the strongest local oxygen-transport limitation downstream. As a result, the previously observed mid-channel minimum becomes less distinct, while the outlet region becomes increasingly dominated by local oxygen-transport limitation.

In contrast to P_{LF2}, P_{LF1} shows almost no systematic change in characteristic frequency along the channel for either wet or dry operation. This agrees with the expectation that the RH variation does not directly alter the mean channel gas velocity, u_{ch}, so that the dominant time scale of P_{LF1} remains largely unchanged. A notable exception occurs at the outlet under dry conditions. At S13, P_{LF1} shifts distinctly to lower frequencies, whereas the corresponding wet-condition peak remains nearly unchanged. Since this frequency shift coincides with the sharp drop in local current density at the last segment, it is interpreted as a local downstream effect rather than as an isolated outlier. Most likely, this behavior reflects water-related changes in effective channel flow and gas-side mass-transfer conditions at the outlet. These changes modify the local channel-related response and lead to an additional slowing of P_{LF1} [16,18].

The main RH effect on P_{LF1} is therefore observed primarily in amplitude rather than in frequency. Under dry conditions, P_{LF1} is already somewhat larger at the inlet. It increases further toward about S4, remains approximately constant up to S10, and decreases again toward S13. In the mid-channel region, self-humidification partly compensates for the initially drier inlet conditions. As a result, the P_{LF1} contributions under dry and wet operation become very similar. Toward the outlet, however, P_{LF1} is somewhat larger under wet conditions. This follows the higher local current density sustained there and the stronger channel-related contribution associated with oxygen consumption. Overall, the RH variation affects P_{LF1} mainly indirectly through the redistribution of electrochemical activity and the resulting coupling between oxygen transport along the channel and local through-plane oxygen diffusion through the porous cathode layers [7,16,17].

4.8. Dependency summary

To summarize, the observed parameter dependencies resolve two distinct low-frequency processes, P_{LF1} and P_{LF2}. In the present cell geometry and operating window, P_{LF1} consistently appears as the lower-frequency peak. Its frequency responds most clearly to channel-gas velocity, as shown by the stoichiometry- and load-dependent changes in convective residence time. Its amplitude, however, is additionally modulated by axial oxygen consumption. It is also influenced by the coupling between oxygen transport along the channel and local through-plane oxygen transport through the porous cathode layers via interfacial mass transfer at the channel-GDL interface, as illustrated in Fig. 1 and described by Eq. (5). P_{LF1} can therefore not be described as a purely convective or conversion-controlled process.

In contrast, P_{LF2} responds most strongly to inert-gas variations and to the local through-plane oxygen-transport conditions in the porous cathode layers, which are determined by the local current-density distribution, oxygen availability, and liquid-water content. The RH dependence observed here is therefore expressed primarily indirectly, via the redistribution of local current density and local water-related transport conditions along the channel. Its characteristic time scale is governed mainly by the effective local through-plane oxygen-transport response, including the transport properties of the porous cathode structure, local oxygen availability, water state, and water-dependent changes in the effective transport domain, as schematically summarized in Fig. 1. Its amplitude reflects the combined effect of local oxygen demand and the severity of the local oxygen-transport limitation under the prevailing operating conditions.

These dependencies support a distinction between P_{LF2} as a predominantly local through-plane oxygen-transport contribution in the porous cathode and P_{LF1} as a predominantly channel-related low-frequency contribution associated with oxygen transport along the channel and its coupling to local porous-cathode transport via the channel–GDL interface. At the same time, both processes remain coupled under technically relevant PEMFC operation.

Table 1 summarizes the observed dependencies and the proposed origins of the low-frequency processes inferred from the parameter variations.

Table 1
Parameter dependencies and presumable origins of identified low-frequency polarization processes.

Process	Observed position in this study	Frequency mainly sensitive to	Amplitude mainly sensitive to	Mechanistic interpretation
P_{LF1}	lower-frequency LF peak	channel gas velocity / residence time, local deviations in u_{ch}	gas transport, liquid-water distribution	channel-related LF process with coupling to local porous-cathode transport
P_{LF2}	higher-frequency LF peak	effective local through-plane O_2 transport time scale, D_{eff}-related gas transport, local hydration and liquid-water distribution	local O_2 demand, local O_2 availability, water-affected through-plane O_2 transport limitation	local through-plane O_2 transport process in the porous cathode

5. Conclusions

In this study, the low-frequency region of the impedance spectrum was investigated under technically relevant PEMFC operation using a segmented cell. This approach enabled the spatially resolved analysis of local low-frequency processes under realistic along-the-channel gradients in oxygen availability, humidity, and water accumulation. By sequential local EIS measurements and subsequent DRT analysis, two distinct low-frequency contributions, P_{LF1} and P_{LF2}, were identified and analyzed over the investigated operating window. Their sensitivities were examined first under controlled conditions at Segment 1 and then under along-the-channel operation by varying inert-gas type, cathode stoichiometry, current density, and relative humidity.

The lower-frequency peak, P_{LF1}, shows its clearest frequency dependence on channel-gas velocity and therefore on parameters that affect the convective residence time, such as cathode stoichiometry and load-dependent flow rate. At the same time, its amplitude cannot be explained by flow rate alone. P_{LF1} increases toward the outlet at low stoichiometry and is also sensitive to operating-state changes at high load. Under He, its amplitude is only slightly reduced near the inlet, but this reduction becomes progressively more pronounced toward the outlet. Together, these observations indicate that P_{LF1} reflects a channel-related process that is additionally shaped by axial oxygen depletion. It is further influenced by the coupling between oxygen transport along the channel and local through-plane oxygen transport through the porous cathode layers via interfacial mass transfer at the channel-GDL interface. Thus, P_{LF1} is not a purely convective or conversion-controlled peak, but a coupled channel-related low-frequency contribution.

The higher-frequency low-frequency peak, P_{LF2}, responds most strongly to changes in local through-plane oxygen-transport conditions in the porous cathode. Its shift to higher frequencies under He demonstrates a strong sensitivity to the effective gas-phase oxygen diffusion coefficient, while its amplitude and frequency change markedly with local current-density redistribution, oxygen availability, and local hydration and liquid-water distribution. Along the channel, P_{LF2} shows the strongest spatial sensitivity, consistently reflecting the local through-plane oxygen-transport limitation in the porous cathode structure. Under wet or dry conditions, its behavior is not determined by hydration alone, but by the combined effect of local oxygen demand, local oxygen availability, ionomer-related oxygen transport, and water-dependent changes in the porous transport domain.

The observed dependencies support a mechanistic distinction between P_{LF2} as a predominantly local through-plane oxygen-transport contribution in the porous cathode layers and P_{LF1} as a predominantly channel-related low-frequency contribution associated with oxygen transport along the channel and its coupling to local through-plane oxygen transport through the porous cathode layers. Depending on operating state, both processes can overlap and appear as a merged low-frequency response, which explains why a single low-frequency peak in PEMFC spectra should not be interpreted as a unique transport mechanism.

6. Declaration of generative AI and AI-assisted technologies in the manuscript preparation process

During the preparation of this work, the authors used ChatGPT 5.4 in order to assist with grammar and language review during the drafting of this manuscript. After using this tool, the authors reviewed and edited the content as needed and take full responsibility for the content of the published article.

CRediT authorship contribution statement

Philipp Oppek: Conceptualization, Data curation, Formal analysis, Investigation, Methodology, Project administration, Resources, Validation, Writing – original draft, Writing – review & editing. **Kersten Schwab:** Formal analysis, Methodology, Validation, Writing – review & editing. **Tobias Goosmann:** Formal analysis, Methodology, Supervision, Validation, Writing – review & editing. **Sebastian Raab:** Validation, Writing – review & editing. **Yannick Fischer:** Investigation, Resources. **Mischa Geörg:** Investigation, Resources. **Tatyana Reshetenko:** Formal analysis, Validation, Writing – review & editing. **André Weber:** Funding acquisition, Resources, Supervision, Validation, Writing – review & editing.

Declaration of competing interest

The authors declare that they have no known competing financial interests or personal relationships that could have appeared to influence the work reported in this paper.

Acknowledgment

The authors gratefully acknowledge funding from the Central Innovation Programme for SMEs (ZIM), funded by the Federal Ministry for Economic Affairs and Energy (BMWK), Germany (BMWK ZIM KK5039609DF4).

Supplementary materials

Supplementary material associated with this article can be found, in the online version, at doi:10.1016/j.electacta.2026.149408.

Data availability

The raw data that has been used is not available due to confidentiality reasons. Data as presented in the figures is available up on request.

References

[1] G.R. Molaeimanesh, F. Torabi, Chapter 1 - Fuel cell fundamentals, in: G. R. Molaeimanesh, F.T. Eds (Eds.), Fuel Cell Modeling and Simulation, Elsevier, 2023, pp. 1–56.
[2] A. Kongkanand, M.F. Mathias, The Priority and Challenge of High-Power Performance of Low-Platinum Proton-Exchange Membrane Fuel Cells, J. Phys. Chem. Lett. 7 (7) (2016) 1127–1137, https://doi.org/10.1021/acs.jpclett.6b00216, 2016/04/07.
[3] E. Fensterle, F. Rabsahl, J. Hunger, F. Wilhelm, J. Scholta, M. Hölzle, Spatially Resolved Current Density and Electrochemical Impedance Spectroscopy in PEM Fuel Cells, Fuel Cells 26 (2) (2026) e70057, https://doi.org/10.1002/fuce.70057, 2026/04/01.
[4] J. Mitzel, et al., Fault Diagnostics in PEMFC Stacks by Evaluation of Local Performance and Cell Impedance Analysis, Fuel Cells 20 (4) (2020) 403–412, https://doi.org/10.1002/fuce.201900193, 2020/08/01.

[5] S. Shimpalee, S. Hirano, M. DeBolt, V. Lilavivat, J.W. Weidner, Y. Khunatorn, Macro-Scale Analysis of Large Scale PEM Fuel Cell Flow-Fields for Automotive Applications, J. Electrochem. Soc. 164 (11) (2017) E3073–E3080, https://doi.org/10.1149/2.0091711jes.

[6] I.S. Hussaini, C.-Y. Wang, Visualization and quantification of cathode channel flooding in PEM fuel cells, J. Power. Sources. 187 (2) (2009) 444–451, https://doi.org/10.1016/j.jpowsour.2008.11.030.

[7] I.A. Schneider, S.A. Freunberger, D. Kramer, A. Wokaun, G.G. Scherer, Oscillations in Gas Channels: part I. The Forgotten Player in Impedance Spectroscopy in PEFCs, J. Electrochem. Soc. 154 (4) (2007) B383, https://doi.org/10.1149/1.2435706, 2007/02/09.

[8] M. Heinzmann, A. Weber, E. Ivers-Tiffée, Advanced impedance study of polymer electrolyte membrane single cells by means of distribution of relaxation times, J. Power. Sources. 402 (2018) 24–33, https://doi.org/10.1016/j.jpowsour.2018.09.004.

[9] T. Reshetenko, A. Kulikovsky, Understanding the distribution of relaxation times of a low–Pt PEM fuel cell, Electrochim. Acta 391 (2021), https://doi.org/10.1016/j.electacta.2021.138954.

[10] P.A. García-Salaberri, P.K. Das, A.M. Chaparro, Local oxygen transport resistance in polymer electrolyte fuel cells: origin, dependencies and mitigation, Front. Energy Res. 12 (2024), https://doi.org/10.3389/fenrg.2024.1357325.

[11] Y. Fukuyama, T. Shiomi, T. Kotaka, Y. Tabuchi, The Impact of Platinum Reduction on Oxygen Transport in Proton Exchange Membrane Fuel Cells, Electrochim. Acta 117 (2014) 367–378, https://doi.org/10.1016/j.electacta.2013.11.179, 2014/01/20/.

[12] A.Z. Weber, M.A. Hickner, Modeling and high-resolution-imaging studies of water-content profiles in a polymer-electrolyte-fuel-cell membrane-electrode assembly, Electrochim. Acta 53 (26) (2008) 7668–7674, https://doi.org/10.1016/j.electacta.2008.05.018, 2008/11/01/.

[13] H. Li, et al., A review of water flooding issues in the proton exchange membrane fuel cell, J. Power. Sources. 178 (1) (2008) 103–117, https://doi.org/10.1016/j.jpowsour.2007.12.068, 2008/03/15/.

[14] M. Chandesris, C. Robin, M. Gerard, Y. Bultel, Investigation of the difference between the low frequency limit of the impedance spectrum and the slope of the polarization curve, Electrochim. Acta 180 (2015) 581–590, https://doi.org/10.1016/j.electacta.2015.08.089.

[15] M. Heinzmann, A. Weber, E. Ivers-Tiffée, Impedance modelling of porous electrode structures in polymer electrolyte membrane fuel cells, J. Power. Sources. 444 (2019), https://doi.org/10.1016/j.jpowsour.2019.227279.

[16] G. Maranzana, et al., A proton exchange membrane fuel cell impedance model taking into account convection along the air channel: on the bias between the low frequency limit of the impedance and the slope of the polarization curve, Electrochim. Acta 83 (2012) 13–27, https://doi.org/10.1016/j.electacta.2012.07.065.

[17] S. Cruz-Manzo, P. Greenwood, Analytical Warburg Impedance Model for EIS Analysis of the Gas Diffusion Layer with Oxygen Depletion in the Air Channel of a PEMFC, J. Electrochem. Soc. 168 (7) (2021), https://doi.org/10.1149/1945-7111/ac1031.

[18] D.K.I.A. Schneider, A. Wokaun, G.G. Scherer, Oscillations in Gas Channels: II. Unraveling the Characteristics of the Low Frequency Loop in Air-Fed PEFC Impedance Spectra, J. Electrochem. Soc. 154 (8) (2007), https://doi.org/10.1149/1.2742291.

[19] S. Keller, et al., Characteristic Time Constants Derived From the Low-Frequency Arc of Impedance Spectra of Fuel Cell Stacks, J. Electrochem. Energy Convers. Storage 15 (2) (2018), https://doi.org/10.1115/1.4038632.

[20] C. Bao, W.G. Bessler, Two-dimensional modeling of a polymer electrolyte membrane fuel cell with long flow channel. Part II. Physics-based electrochemical impedance analysis, J. Power. Sources. 278 (2015) 675–682, https://doi.org/10.1016/j.jpowsour.2014.12.045.

[21] A. Kulikovsky, Analytical Impedance of Oxygen Transport in a PEM Fuel Cell Channel, J. Electrochem. Soc. 166 (4) (2019) F306–F311, https://doi.org/10.1149/2.0951904jes.

[22] S. Chevalier, C. Josset, B. Auvity, Analytical solution for the low frequency polymer electrolyte membrane fuel cell impedance, J. Power. Sources. 407 (2018) 123–131, https://doi.org/10.1016/j.jpowsour.2018.10.039.

[23] T. Schmitt, R. Bligny, G. Maranzana, J. Dillet, U. Sauter, An Experimental Study of Humidity Distribution Dynamics in a Segmented PEM Fuel Cell, J. Electrochem. Soc. 169 (12) (2022), https://doi.org/10.1149/1945-7111/aca720.

[24] T. Reshetenko, A. Kulikovsky, Variation of PEM Fuel Cell Physical Parameters with Current: impedance Spectroscopy Study, J. Electrochem. Soc. 163 (9) (2016) F1100–F1106, https://doi.org/10.1149/2.0981609jes.

[25] X. Liu, W. Tao, Z. Li, Y. He, Three-dimensional transport model of PEM fuel cell with straight flow channels, J. Power. Sources. 158 (1) (2006) 25–35, https://doi.org/10.1016/j.jpowsour.2005.08.046, 2006/07/14/.

[26] Y. Wang, S. Basu, C.-Y. Wang, Modeling two-phase flow in PEM fuel cell channels, J. Power. Sources. 179 (2) (2008) 603–617, https://doi.org/10.1016/j.jpowsour.2008.01.047, 2008/05/01/.

[27] T. Sakai, H. Takenaka, E. Torikai, Gas Diffusion in the Dried and Hydrated Nafions, J. Electrochem. Soc. 133 (1) (1986) 88, https://doi.org/10.1149/1.2108551, 1986/01/01.

[28] A. Kulikovsky, Analytical Impedance of Oxygen Transport in the Channel and Gas Diffusion Layer of a PEM Fuel Cell, J. Electrochem. Soc. 168 (11) (2021), https://doi.org/10.1149/1945-7111/ac3a2d.

[29] J.H. Nam, M. Kaviany, Effective diffusivity and water-saturation distribution in single- and two-layer PEMFC diffusion medium, Int. J. Heat. Mass Transf. 46 (24) (2003) 4595–4611, https://doi.org/10.1016/s0017-9310(03)00305-3.

[30] U. Pasaogullari, C.Y. Wang, Liquid Water Transport in Gas Diffusion Layer of Polymer Electrolyte Fuel Cells, J. Electrochem. Soc. 151 (3) (2004) A399, https://doi.org/10.1149/1.1646148, 2004/02/05.

[31] H. Fathi, A. Raoof, S.H. Mansouri, M.T. van Genuchten, Effects of Porosity and Water Saturation on the Effective Diffusivity of a Cathode Catalyst Layer, J. Electrochem. Soc. 164 (4) (2017) F298, https://doi.org/10.1149/2.0871704jes, 2017/02/08.

[32] T. Reshetenko, Y. Sun, T. Kadyk, M. Eikerling, A. Kulikovsky, An impedance spectroscopy study to unravel the effect of water on proton and oxygen transport in PEM fuel cells, Electrochim. Acta 507 (2024) 145172, https://doi.org/10.1016/j.electacta.2024.145172, 2024/12/10/.

[33] S. Chevalier, C. Josset, A. Bazylak, B. Auvity, Measurements of Air Velocities in Polymer Electrolyte Membrane Fuel Cell Channels Using Electrochemical Impedance Spectroscopy, J. Electrochem. Soc. 163 (8) (2016) F816–F823, https://doi.org/10.1149/2.0481608jes.

[34] K. Min, S. Kang, F. Mueller, J. Auckland, J. Brouwer, Dynamic Simulation of a Stationary Proton Exchange Membrane Fuel Cell System, J. Fuel. Cell Sci. Technol. 6 (4) (2009), https://doi.org/10.1115/1.3008029.

[35] S. Kang, K. Min, F. Mueller, J. Brouwer, Configuration effects of air, fuel, and coolant inlets on the performance of a proton exchange membrane fuel cell for automotive applications, Int. J. Hydrog. Energy 34 (16) (2009) 6749–6764, https://doi.org/10.1016/j.ijhydene.2009.06.049, 2009/08/01/.

[36] Y. Ding, et al., Characterizing the two-phase flow effect in gas channel of proton exchange membrane fuel cell with dimensionless number, Int. J. Hydrog. Energy 48 (13) (2023) 5250–5265, https://doi.org/10.1016/j.ijhydene.2022.09.288, 2023/02/12/.

[37] R. Wu, et al., Determination of oxygen effective diffusivity in porous gas diffusion layer using a three-dimensional pore network model, Electrochim. Acta 55 (24) (2010) 7394–7403, https://doi.org/10.1016/j.electacta.2010.07.018, 2010/10/01/.

[38] M. Koz, S.G. Kandlikar, Oxygen transport resistance at gas diffusion layer – Air channel interface with film flow of water in a proton exchange membrane fuel cell, J. Power. Sources. 302 (2016) 331–342, https://doi.org/10.1016/j.jpowsour.2015.10.080, 2016/01/20/.

[39] M. Heinzmann, A. Weber, Impedance based performance model for polymer electrolyte membrane fuel cells, J. Power. Sources. 558 (2023), https://doi.org/10.1016/j.jpowsour.2022.232540.

[40] T. Goosmann, Impedanzbasierte, Mehrdimensional Ortsaufgelöste Prädiktion des Betriebsverhaltens von PEM-Brennstoffzellenstacks," Ph.D. Thesis, Karlsruher Institut für Technologie (KIT), 2025, https://doi.org/10.5445/IR/1000185312 [Online]. Available.

[41] F. Haimerl, J.P. Sabawa, T.A. Dao, A.S. Bandarenka, Spatially Resolved Electrochemical Impedance Spectroscopy of Automotive PEM Fuel Cells, ChemElectroChem 9 (10) (2022), https://doi.org/10.1002/celc.202200069.

[42] Freudenberg Performance Materials SE & Co. KG, "Freudenberg Gas Diffusion Layers—Technical Data," Weinheim, Germany, 2020.

[43] M. Schönleber, D. Klotz, E. Ivers-Tiffée, A Method for Improving the Robustness of linear Kramers-Kronig Validity Tests, Electrochim. Acta 131 (2014) 20–27, https://doi.org/10.1016/j.electacta.2014.01.034, 2014/06/10/.

[44] H. Schichlein, A.C. Müller, M. Voigts, A. Krügel, E. Ivers-Tiffée, Deconvolution of electrochemical impedance spectra for the identification of electrode reaction mechanisms in solid oxide fuel cells, J. Appl. Electrochem. 32 (8) (2002) 875–882, https://doi.org/10.1023/A:1020599525160, 2002/08/01.

[45] A.-N. Tikhonov, A.V. Goncharsky, V.V. Stepanov, A.G. Yagola, Numerical methods for the approximate solution of ill-posed problems on compact sets. Numerical Methods for the Solution of Ill-posed problems, Springer, 1995, pp. 65–79.

[46] T. Reshetenko, A. Kulikovsky, Distribution of Relaxation Times: a Tool for Measuring Oxygen Transport Resistivity of a Low–Pt PEM Fuel Cell Cathode, J. Electrochem. Soc. 167 (14) (2020), https://doi.org/10.1149/1945-7111/abc10f.

[47] A. Tanaka, K. Nagato, M. Tomizawa, G. Inoue, K. Nagai, M. Nakao, Advanced impedance modeling for micropatterned polymer electrolyte membrane fuel cells, J. Power. Sources. 545 (2022) 231937, https://doi.org/10.1016/j.jpowsour.2022.231937, 2022/10/15/.

[48] S. Raab, A. Karmakar, P.-Y.A. Chuang, A. Weber, Effect of Ionomer-to-Carbon Ratio on PEMFC Carbon Corrosion: an Electrochemical Study, J. Electrochem. Soc. 172 (11) (2025) 114508, https://doi.org/10.1149/1945-7111/ae1b3d, 2025/11/18.

[49] S. Raab, A. Weber, Impedance-based analysis of PEMFC degradation phenomena during accelerated stress tests, J. Power. Sources. 673 (2026) 239725, https://doi.org/10.1016/j.jpowsour.2026.239725, 2026/05/01/.

[50] A. Tanaka, G. Inoue, K. Nagato, Impedance modeling of PEM fuel cells incorporating catalyst-layer heterogeneity, J. Power. Sources. 663 (2026), https://doi.org/10.1016/j.jpowsour.2025.238876.

[51] E.A. Chadwick, B. Derebasi, V.P. Schulz, A. Bazylak, Influence of gravity on water management and mass transport losses in polymer electrolyte membrane fuel cells, Sci. Rep. 15 (1) (2025) 39380, https://doi.org/10.1038/s41598-025-09067-y.

[52] S. Primdahl, M. Mogensen, Gas Diffusion Impedance in Characterization of Solid Oxide Fuel Cell Anodes, J. Electrochem. Soc. 146 (8) (1999) 2827, https://doi.org/10.1149/1.1392015, 1999/08/01.

[53] T. Jacobsen, P.V. Hendriksen, S. Koch, Diffusion and conversion impedance in solid oxide fuel cells, Electrochim. Acta 53 (25) (2008) 7500–7508, https://doi.org/10.1016/j.electacta.2008.02.019, 2008/10/30/.